A high-efficiency regime for gas-phase terahertz lasers

Fan Wang[a,b,1], Jeongwon Lee[b], Dane J. Phillips[c], Samuel G. Holliday[c], Song-Liang Chua[d], Jorge Bravo-Abad[e], John D. Joannopoulos[b,f,1], Marin Soljačić[b,f], Steven G. Johnson[b,f,g,1], and Henry O. Everitt[h,i,1]

[a]Department of Mechanical Engineering, Massachusetts Institute of Technology, Cambridge, MA 02139; [b]Research Laboratory of Electronics, Massachusetts Institute of Technology, Cambridge, MA 02139; [c]IERUS Technologies, Huntsville, AL 35805; [d]Defense Science Organization National Laboratories, Singapore 118225 Singapore; [e]Departamento de Física Teórica de la Materia Condensada and Condensed Matter Physics Center, Universidad Autónoma de Madrid, 28049 Madrid, Spain; [f]Department of Physics, Massachusetts Institute of Technology, Cambridge, MA 02139; [g]Department of Mathematics, Massachusetts Institute of Technology, Cambridge, MA 02139; [h]Department of Physics, Duke University, Durham, NC 27708; and [i]Army Aviation & Missile Research, Development, and Engineering Center, Redstone Arsenal, AL 35898

We present both an innovative theoretical model and an experimental validation of a molecular gas optically pumped far-infrared (OPFIR) laser at 0.25 THz that exhibits $10\times$ greater efficiency (39% of the Manley–Rowe limit) and $1,000\times$ smaller volume than comparable commercial lasers. Unlike previous OPFIR-laser models involving only a few energy levels that failed even qualitatively to match experiments at high pressures, our ab initio theory matches experiments quantitatively, within experimental uncertainties with no free parameters, by accurately capturing the interplay of millions of degrees of freedom in the laser. We show that previous OPFIR lasers were inefficient simply by being too large and that high powers favor high pressures and small cavities. We believe that these results will revive interest in OPFIR laser as a powerful and compact source of terahertz radiation.

optically pumped far-infrared laser | terahertz source | continuous wave gas laser | laser modeling | rotational population inversion

For many years, optically pumped far-infrared (OPFIR) gas lasers were the most powerful sources of continuous-wave (CW) terahertz radiation (1–13), and such terahertz sources are crucial to a wide variety of sensing and imaging applications (14–16). They employ population inversions excited in molecule-specific rotational–vibrational transitions by a line-tunable CO_2 laser. By changing the gas, isotope, and CO_2 laser line, different transition frequencies could be made to lase, typically in meter-long cavities operated at low pressures (<0.1 Torr) and producing up to 100 mW in a manner that depended strongly on the rotational transition involved (https://www.edinst.com/products/; ref. 17). Initially, it was thought that low pressures and large cavities were required, but this produced a "vibrational bottleneck": diffusion-limited relaxation by molecule–wall collisions that filled the vibrational level and quenched any inversion above a maximum pressure, regardless of the pump intensity (2, 4, 6). It was subsequently discovered that OPFIR lasers could operate at pressures higher than this in smaller cavities, a result of collisional processes that excited high-energy vibrational levels and removed the bottleneck (7, 9). This breakthrough was never fully investigated or exploited, however, as it came at a time when new sources of terahertz radiation were emerging (18–20) and the use of OPFIR lasers was waning due to their supposed large sizes (e.g., 10 cm in diameter and 1 m in length) and low photon conversion efficiencies (e.g., 0.1–10%).

The advent of alternatives to line-tunable CO_2 lasers (21, 22) and the increasing need for powerful, narrowband sources of terahertz radiation are reviving interest in compact OPFIR lasers (13), whose full potential has never been fully understood because of the thousands of quantized states involved and the millions of collision cross-sections required to simulate its behavior adequately. In fact, all previous OPFIR-laser models involving only a few vibrational levels exhibited unphysical bottlenecking at high pressures and failed even qualitatively to match experiments (2–4, 13).

Here, we present both experiments and an innovative theoretical model that not only match at all pressures, but also exhibit unprecedented conversion efficiencies and device compactness. We solve deficiencies of earlier models by developing a far more complete theory for a compact OPFIR laser, using the prototypical molecular gas $^{13}CH_3F$ pumped by a line-tunable CO_2 laser (Fig. 1). Using no adjustable parameters, our model matches our experimental measurements (Fig. 2) with excellent accuracy, especially considering its sensitivity to many experimental variables. The critical part of our theory is an effective vibrational temperature that includes all accessible high-lying vibrational levels without having to describe the relaxation processes among them explicitly. Moreover, our ab initio theory accurately captures the interplay of millions of population degrees of freedom in the laser, including many collisional processes that other researchers neglected or approximated, such as inhomogeneous broadening, dipole–dipole collisions, symmetry-preserving thermalization, V-swap processes, molecule–wall collisions, velocity subclasses, and spatial diffusion. An efficient numerical solver is developed to find the steady state directly, without time evolution, as a system of millions of coupled nonlinear rate equations. Not only does the model match experiments; it also unexpectedly shows that our compact laser exhibits remarkable conversion efficiency, up to 39% of the Manley–Rowe (23) limit. Our compact laser is $1,000\times$ smaller in volume while delivering more than

Significance

Optically pumped far-infrared (OPFIR) lasers are one of the most powerful continuous-wave terahertz sources. However, such lasers have long been thought to have intrinsically low efficiency and large sizes. Moreover, all previous theoretical models failed to predict even qualitatively the experimental performance at high pressures. Here, we have developed an innovative model that captures the full physics of the lasing process and correctly predicts the behavior in the high-pressure regime. Validated against experiments, our model shows that nearly all previous OPFIR lasers were operating in the wrong regime and that $10\times$ greater efficiency is possible by redesigning the terahertz cavity. Our results reintroduce the use of OPFIR lasers as a powerful and compact source of terahertz radiation.

ENGINEERING

Fig. 1. (*A* and *B*) Schematics of (*A*) the laser cavity and (*B*) molecular energy levels of $^{13}CH_3F$. The cavity is a copper tube with a movable back wall used to tune the cavity frequency to match the laser gain, pumped with an IR laser through a pinhole in the front window. The energy levels consist of vibrational levels V_ℓ, with A and E symmetries (10), composed of rotational levels with quantum numbers J and K. The IR pump excites a transition between levels L and U as shown, and lasing occurs for both the direct inversion between U and U − 1 and the refilling inversion between L + 1 and L.

$10\times$ greater efficiency than the best commercial OPFIR lasers (Fig. 3). Finally, we explore and optimize the cavity geometry (Fig. 4) to achieve even greater output terahertz power over a much wider range of gas pressures. We believe that these findings will revive interest in OPFIR lasers as high-power, compact, continuous-wave terahertz sources.

Experimental Measurements

Fig. 1 depicts our OPFIR laser: A line-tunable CO_2 pump laser ($\lambda = 9.7 \mu m$) is focused through a pinhole in the front copper mirror into a 5-mm × 14.3-cm copper tube filled with $^{13}CH_3F$ gas. The lasing transition is brought into resonance with the cavity by a copper-plunger rear mirror that adjusts the cavity length, and the resulting laser power emerges from the same pinhole, after which it is detected by a heterodyne receiver. The different rotational levels are characterized by a rotational quantum number J, its projection quantum number K, and the vibrational state V_ℓ to which it belongs (24, 25). For symmetric-top molecules,

there are two nuclear spin-dependent symmetry types, A and E (10, 24). In $^{13}CH_3F$, the coincidence between the 9P(32) line of the pump laser and the $R_3(4)$ ro-vibrational transition in $^{13}CH_3F$ produces two rotational population inversions, the "direct" $J = 5 \rightarrow 4$ (with $K = 3$, type A) inversion in V_3 with frequency 245.351 GHz and a corresponding "refilling" rotational transition in the type A ground vibrational level V_0 with frequency 248.559 GHz (Fig. 1) (13). The heterodyne receiver distinguishes the lasing transitions and measures their intensity as a function of pressure and the input pump power. Fig. 2 shows that the refilling transition produces the most terahertz power in a manner that depends nonlinearly on the input pump power, but the direct inversion survives over a much broader range of pressures. In contrast with previous theoretical models that predicted a pump power-independent vibrational bottleneck, these pressure-dependent and pump power-dependent behaviors in our compact OPFIR laser show no vibrational bottleneck on either transition. In fact, increasing pump power produces higher-pressure operation, indicating even stronger emission and higher pressures are achievable.

Ab Initio Modeling

To understand the lack of vibrational bottlenecking, a thorough model of OPFIR laser operation must capture many different physical processes. Gas-phase molecules typically have hundreds to thousands of thermally populated rotational energy levels in the same vibrational modes as the pumped states ($L \rightarrow U$). It has previously been shown that rapid collisional thermalization maintains a Boltzmann distribution of population across most rotational states within a given vibrational level V_ℓ and symmetry type (A or E); consequently, they may be modeled as a thermal pool (5, 8–10). This thermal-pool approximation dramatically simplifies models of the collision physics by reducing the number of levels that must be individually included and collision cross-sections that must be known to those few most closely connected to L and U. Nevertheless, after the pump excites molecules from L to U, a complicated set of collisional relaxation processes ensues, both bimolecular rotational energy transfer and molecular diffusion to the walls for ro-vibrational thermalization, so that population inversions between L + 1 and L (refilling) and U and U − 1 (direct) occur in a manner that depends sensitively on the input pump power, pressure, radial population distribution, cavity length, and cavity mode. Because wall collisions are the primary pathway for vibrational relaxation in OPFIR lasers and the diffusion rate goes as $1/pR^2$ for pressure p and cell radius R, typical large-diameter glass OPFIR lasers require operation at low pressure, while small-diameter metallic cells are favored for high-pressure operation (with the tradeoff of increased ohmic losses at the lasing frequency).

Various models have been developed in an attempt to understand the inversion process (2–4, 13). A troubling limitation in all these models, shown in *SI Appendix*, Fig. S2, was that they exhibited an unphysical bottlenecking of the inversion at high pressures, regardless of the input pump power. Consequently, they were unable to explain high-pressure lasing such as that shown in Fig. 2. Ref. 7 addressed the problem of high-pressure bottlenecking by including more vibrational levels; however, that model was too oversimplified and incomplete to provide useful quantitative guidance for cavity design, and the lack of an efficient numerical solver prohibited any attempt at a more realistic model.

Retaining the spirit of ref. 7, we construct a far more complete model that quantitatively describes how this unphysical bottlenecking is overcome through the collisional excitation of molecules into hundreds of excited vibrational levels in compact OPFIR lasers. In our model, whose complete mathematical details are provided in *SI Appendix*, section 1: Experimental Measurements and Theoretical Modeling, the degrees of

Fig. 2. (*A*) Experimental and (*B*) theoretical terahertz laser output power as a function of gas pressure, for various input pump powers (3.3 W, 6.6 W, and 10 W) and for both the direct (solid lines) and refilling (dashed lines) transitions. Excellent agreement is obtained even though the theoretical model has no adjustable parameters; in contrast to previous work (2–4, 13), our theory captures the fact that higher powers allow operation at higher pressures, in part because of an innovative technique to model a large number of high-energy vibrational levels. The dotted parts of the direct lasing curves represent an inefficient regime in which the pump intensity is nearly zero in the back of the cavity. In this case our model's approximation of an effective z-uniform pump strength is inaccurate, but it is not desirable to operate in

freedom in the rate equations include axial molecular speed v, radial position r, time t, and different energy levels including nonthermal rotational levels and vibrational thermal pools. By calculating separate populations at each v, unlike previous work, we can accurately model inhomogeneous broadening and spectral hole burning (SHB) effects on the Doppler-broadened pumped IR transition and the resulting pressure-broadened terahertz gain profile. By additionally modeling each population density as a function of r, the overlap between the inversion and the cavity mode is calculated for an accurate estimation of the weighted gain coefficient. In the efficient regime where the pump intensity reaches the entire cavity (i.e., IR absorption, spectral hole burning, and saturation effects do not cause the pump intensity to decay strongly before reaching the end of the cavity), the populations can be approximated as uniform in z with an effective z-averaged pump intensity (different from the input pump intensity, *SI Appendix*, section 2: More Technical Details), which greatly simplifies the calculations.

Given a set of nonlinear rate equations, most authors evolve them in time until the steady state is obtained (9, 13), but this approach is severely inefficient, especially at high pressures where timescales for different relaxation processes diverge widely. Instead, we solve for the steady state directly, without time evolution, as a system of millions of coupled nonlinear equations, with computational cost equivalent to less than 100 time-evolution steps. This enormous computational improvement allows us to include not only millions of population degrees of freedom but also many physical processes that other authors neglected or approximated. In particular, we include dipole–dipole collisions between rotational states (12), symmetry-preserving thermalization (SPT) (also called K-swap processes) between nonthermal rotational states and vibrational thermal pools, the V-swap process (10, 24), nonresonant collisions among thermal pools (24, 25), molecule–wall collisions (9, 13), and spatial diffusion (13). For the inhomogeneously broadened pump absorption (25), we include Doppler, AC-Stark (26), and pressure (23) broadening of velocity subclasses, and we determine the average pump intensity self-consistently, including SHB and pump saturation, with the absorption coefficient calculated from the populations. Given rate equations for the populations $N_k(v, r, t)$ of each level k (*SI Appendix*, section 1: Experimental Measurements and Theoretical Modeling), by setting $\partial N_k/\partial t = 0$ we obtain a nonlinear system of equations for the steady-state populations $N_k(v, r)$. From the calculated radially dependent population inversions, gain profiles, and lasing mode geometry, the output of the model is the predicted lasing power I_o, calculated using modified standard formulas (23) with a self-consistent characteristic time as described in *SI Appendix*, section 1: Experimental Measurements and Theoretical Modeling.

Even with the thermal pool simplification and steady-state computation efficiency, the sheer complexity of the inversion process makes it extremely challenging to model accurately. Previous models needed to make many simplifying assumptions, and the reason they produced unphysical bottlenecking at high pressures was conjectured to be their inclusion of only two key vibrational levels (7, 9), e.g., V_0 and V_3 for $^{13}CH_3F$. We confirmed this conjecture with our model by artificially "turning off" collisional processes one by one. The only process that circumvented vibrational bottlenecking was the process by which higher-lying vibrational levels are populated. The difficulty of including these higher-lying vibrational levels seems almost

this regime. Our model also predicts (*C*) the input pump power at lasing threshold (blue) and the differential quantum efficiency (DQE) (yellow) (23) normalized by the Manley–Rowe (MR) limit at threshold vs. pressure for both inversions. The refilling inversion is both higher power and higher efficiency, with a modeled DQE that can reach 64%.
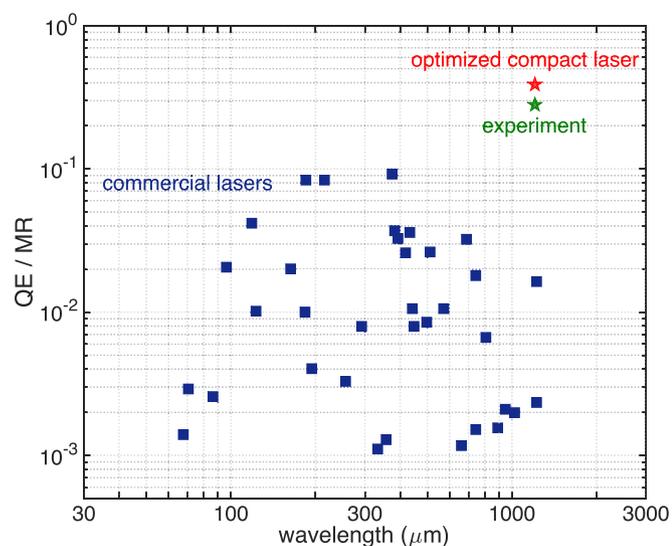
Fig. 3. Total quantum efficiency (23) (QE = THz power out/IR power in) of commercial OPFIR lasers (https://www.edinst.com/products/) and our compact OPFIR laser, normalized by the MR limit (23) on QE. Our experimentally demonstrated laser achieves a QE that is 29% of the MR limit (29% of 0.8%) which improves to 39% after cavity optimization. Both are 10× better than the best commercial laser at the same frequency (0.25 THz or 1.2 mm wavelength), while being 1,000× smaller—in fact, we show theoretically that this efficiency boost is mainly due to the fact that our cavity is so much smaller.

insurmountable at first: Although the energies of hundreds of vibrational levels are known (25), the relaxation processes among them are not known quantitatively and are infeasible to measure. To deal with that problem, a crucial theoretical innovation of our work is to describe those levels implicitly via an effective temperature (different from the ambient temperature!) that is determined self-consistently from the few collisional cross-sections whose values are known. Specifically, we make the ansatz that vibrational transitions are rapid enough to "thermalize" those levels with a Boltzmann distribution described by an effective temperature T_v, so they may be grouped together into separate population pools V_Σ for the A and E symmetries, as shown in Fig. 1B. This is similar to the experimentally justified thermal-pool assumption (8, 10) that maintains a constant temperature among rotational states within a given symmetry type and vibrational level. The main justification of this ansatz is that thermalization among vibrational states is through bimolecular collisions, meaning the rates increase with pressure, while vibrational-state relaxation occurs through diffusion to the walls, which goes as the inverse of pressure. Therefore, the higher the pressure, the more vibrational thermalizing collisions occur before diffusion to the walls relaxes the excitation, and so our model becomes more accurate precisely in the high-pressure regime where these extra vibrational levels are relevant to the inversion.

To implement this thermalization ansatz, the populations of V_0 and V_3 are calculated explicitly, and we then assign the effective temperature of the remaining vibrational levels to be $T_v = (E_{V_3} - E_{V_0})/k_B \log(N_{V_3}/N_{V_0})$, where E_{V_ℓ} and N_{V_ℓ} are the energy and population of level V_ℓ. T_v must be determined self-consistently by our nonlinear solver, simultaneously with N_{V_3} and N_{V_0}, because any population assigned to N_{V_Σ} according to T_v is removed from N_{V_3} and N_{V_0}. If we replace these effective vibrational levels with an explicit six-level model [or even a three-level model as in previous work (2–4, 13)], but include all of the other processes of our model, we find the return of the vibrational bottleneck as in previous work: The inversion disappears above 700 mTorr for all input pump powers

(*SI Appendix*, Fig. S2). Therefore, we confirm the conjecture that including a complete set of vibrational levels through V_Σ eliminates high-pressure bottlecking. Indeed, Fig. 2 shows excellent agreement between the experimentally measured power (Fig. 2A) and the predictions of our model (Fig. 2B), with no free parameters except for the overall scaling, even for pressures >1 Torr where previous models exhibited bottlenecking. In comparing the experimental results to the theoretical model, it is important to keep in mind that there are significant experimental variabilities that limit reproducibility. Among the largest sources of variability are $\sim \pm 10$-MHz drift in the pump frequency offset, $\sim \pm 2$-μm drift in cavity length from the optimal for a given terahertz inversion, and $\sim 10\%$ rise in the cavity pressure over the course of a measurement. A final source of variability is that the optimal tuning for the refilling transition is different from that for the direct transition. Given these
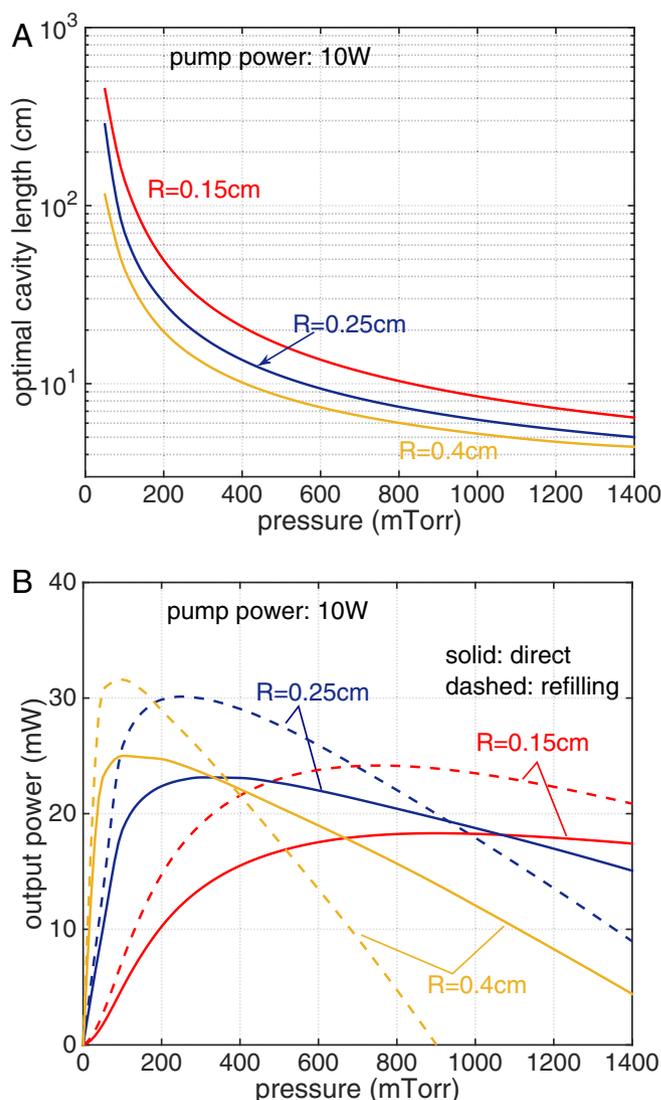
Fig. 4. Theoretical predictions of (A) the roughly optimal cavity length for various radii and (B) the optimized laser output power, both as a function of pressure for an input pump power of 10 W. The cavity length is optimized to equal half the decay length of the pump beam. The output power (B) is shown for the optimal cavity length at each pressure and radius so that each data point is a separate cavity design. The peak efficiency is increased from 29% of MR in the experimental cavity to 39%, but more importantly this optimization allows efficient operation at a wider range of high pressures and hence in smaller cavities.

variabilities, the excellent, roughly quantitative agreement with our model provides striking confirmation of its validity (Fig. 2).

In the dotted parts of Fig. 2B, the pump is highly focused in the front of the cavity and quickly decays to nearly zero (<2%) by the back of the cavity, in which case our model's approximation of an effective z-uniform pump strength is inaccurate, and hence the slight mismatch with experiment is unsurprising. Accurately modeling this attenuated-pump regime is relatively unimportant because, as described below, that regime "wastes" the end of the cavity, and it is preferable to use a shorter cavity.

Since the lasing-mode pattern could not be observed directly in the experiment, we compute the terahertz cavity loss (*SI Appendix*, section 1: Experimental Measurements and Theoretical Modeling) from the lowest-lost [TE$_{01}$ (27)] mode for all curves except for the refilling lasing with input pump power 6.6 W. The 6.6-W experimental refilling curve exhibited a jump in amplitude compared with adjacent powers. We deduce that this is due to a different mode being excited by a mistuned cavity—using the cavity loss and mode profile from the TE$_{22}$ mode produced the best fit to the data. In this way, the accuracy of the model enables us to determine which mode is lasing without directly measuring the mode profile.

Operating OPFIR laser sources at high pressures also leads to an unusually broad and flat gain profile, as shown in *SI Appendix*, Fig. S6. The width of this pressure-broadened gain profile is proportional to the gas pressure (23), as described in *SI Appendix*, section 2: More Technical Details. Such flat gain profiles potentially allow the terahertz lasing frequency to be tuned over a correspondingly broad range ($\sim \pm 10$ MHz at a few hundred millitorrs) without sacrificing efficiency.

Lasing Efficiencies

The agreement between theory and experiment allows us to use the theory to assess the attainable quantum efficiency of the laser accurately and quantitatively, a parameter which was difficult to measure in our experiment because only a fraction of the emitted photons were detected by our heterodyne receiver (*SI Appendix*, section 1: Experimental Measurements and Theoretical Modeling). Fig. 2C plots the predicted lasing threshold and DQE at the threshold, defined as $\eta_d = \frac{dP_{\text{out}}}{dP_{\text{pump}}} / \frac{\nu_{\text{out}}}{\nu_{\text{pump}}}$. Fig. 2C shows that the direct transition has a lower pump threshold, but its DQE is smaller than the refilling transition (which can reach as high as 64%). We also obtain the total quantum efficiency (QE), defined as $\eta_t = \frac{P_{\text{out}}}{P_{\text{pump}}} / \frac{\nu_{\text{out}}}{\nu_{\text{pump}}}$, which is theoretically bounded by 100% from the MR limit (23): The highest achievable power conversion efficiency is the ratio of output and pump frequencies. Our computed QE can be as high as 29% at 350 mTorr for the refilling transition and, as explained below, can increase to 39% in an optimized cavity. As shown in Fig. 3, both QE values are considerably larger than those attained in previous commercial OPFIR lasers.

The remarkably high QE and DQE are an unexpected benefit of high-pressure operation, especially for the refilling transition. The model indicates that as pressure increases, T_v also increases as more of the pumped molecules are collisionally transferred from V$_3$ to V$_\Sigma$ and are therefore removed from the V$_0$ and V$_3$ A-type thermal pools that quench the refilling and direct inversions, respectively. DQE measures the likelihood that each additional pump photon just above threshold produces an additional terahertz photon, and the high DQEs seen at the highest operational pressures mean that both inversions are increasingly efficient as bottlenecking traps molecules in higher vibrational levels. In other words, below threshold most pumped molecules are quickly lost from the levels associated with the inversions due to rapid collisional thermalization, but just above threshold for a given pressure, sufficient collisional redistribution and equilibration of population have been achieved that additional

pump photons simply add to the strength of the inversions. This is particularly true for the refilling transition, where the inversion with L + 1 is produced as the pump laser removes molecules from L. The efficiency of the direct transition is lower and less sensitive to pressure because the pumped molecules placed in U are quickly removed by collisional processes. Consequently, the model indicates that it is the refilling transitions, not the direct transitions typically used in traditional OPFIR lasers, that are most attractive for compact, high-pressure, efficient OPFIR lasers.

Cavity Optimization

With this full understanding of the lasing physics at all pressures, we can finally explore and optimize the cavity geometry to maximize the THz power for compact OPFIR lasers. In particular, we consider the choice of cavity length and radius. Performing parameter variation with our model indicates that output power is maximized by a cavity length of roughly $1/2\alpha_p$, where α_p is the average pump absorption coefficient (*SI Appendix*, section 2: More Technical Details), so here we define $L_o = 1/2\alpha_p$ to be the "optimal" cavity length. Fortunately, operating with this cavity length also ensures the validity of our z-averaged pump-intensity approximation, since L_o is several times smaller than the length where this approximation begins to fail due to nonuniform pump intensity. Calculating L_o is nontrivial because α_p itself depends on cavity length (*SI Appendix*, section 2: More Technical Details), so L_o must be obtained by a self-consistent nonlinear search.

Fig. 4A shows the optimal cavity length as a function of pressure with three different radii R= 0.15 cm, 0.25 cm, and 0.4 cm, with pump power set at 10 W. Because pump absorption increases with increasing pressure, we can see that higher pressures favor shorter cavities. The increase in optimal cavity length with decreasing cavity diameter derives from the increasing pump intensity, the associated increase in AC-Stark broadening and SHB, and the increasing saturation of the pumped L → U transition for a given input pump power. Given that our cavity length was maintained at approximately 14.3 cm for all our measurements, the model indicates that the experimental drop in OPFIR laser power with increasing pressure is caused in part by excess cavity length and incomplete pumping of the entire volume. Another design improvement can be achieved by placing the front pinhole at an optimized position: One chooses the pinhole location to increase the output flux of the lasing mode, which increases both the output power and the efficiency by decreasing the fraction of power lost to ohmic absorption. For example, the TE$_{01}$ mode (27) has a maximum flux intensity around $r = 0.48R$, so an off-center pinhole will achieve larger lasing power, as shown schematically in Fig. 1A. We compute the effect of the pinhole location by calculating the TE$_{01}$ flux through the hole in *SI Appendix*, section 2: More Technical Details.

With the input pump power set at 10 W, the predicted output power for cavities of optimized length and pinhole position is shown in Fig. 4B. Comparison with Fig. 2 A and B indicates how severely the high-pressure lasing is hampered by excess cavity length. For optimized cavities, the maximum output power can reach 31 mW, which is 39% of the MR limit. Cavities with a larger radius of $R = 0.4$ cm can achieve slightly higher output power at low pressures (around 100 mTorr). However, low pressure indicates longer cavity length (around 50 cm) from Fig. 4A. In contrast, 0.15-cm diameter cavities shorter than 20 cm can generate output power about 25% of the MR limit in a wide range of pressure above 400 mTorr. This requirement for widely adjustable cavity lengths is in stark contrast to traditional fixed-geometry OPFIR lasers, typically 10 cm in diameter and 1 m in length (https://www.edinst.com/products/). Our analysis explains why these huge cavities are inefficient, can operate only at very low pressures, and may not be long enough!

Concluding Remarks

Our compact laser is 1,000× smaller in volume while delivering 10× greater efficiency than previous OPFIR lasers at this wavelength. This is shown in Fig. 3, where the QE normalized by the MR limit is plotted for both our experimental setup and our optimized compact laser, as well as for the best commercial OPFIR lasers. The MR limit indicates that for a given input pump power and quantum efficiency, output power increases linearly with decreasing lasing wavelength, so our analyses suggest that future OPFIR lasers can produce even higher powers with a careful choice of cavity and gas. Moreover, we have only scratched the surface of the design possibilities offered by our ability to model the full physics of OPFIR lasers accurately, and we believe that many further discoveries await the extension of our approach to other gases (such as CO and N_2O, e.g., for other wavelengths), other transitions (e.g., for line-tunable operation), and other cavity designs.

Materials and Methods

The experimental procedure, as depicted in Fig. 1 and described in more detail in *SI Appendix*, section 1: Experimental Measurements and Theoretical Modeling, used a sealed 14.3×0.5-cm OPFIR laser cavity, filled with $^{13}CH_3F$ gas, that was pumped by a CO_2 laser at $\lambda = 9.657 \ \mu m$. For each pump power and pressure, a copper plunger in the rear of the tube was adjusted to tune the terahertz cavity resonance to either the direct or the refilling transition, and the resulting terahertz emission was measured by a heterodyne receiver.

Our theoretical model consists of a set of rate equations giving $\dot{N} = \partial N/\partial t$ for both nonthermal rotational populations N_ℓ^r and nonequilibrium populations of vibrational thermal pools N_ρ^v. The theoretical goal is to predict these differences N from the equilibrium (unpumped) populations and their consequences for terahertz gain. In *SI Appendix*, section 1: Experimental Measurements and Theoretical Modeling, these rate equations (which include various transitions, coupling to the pump, diffusion, and an effective-temperature model for unknown vibrational levels), how the $\dot{N} = 0$ steady state is found, and finally how the output power is extracted self-consistently from the populations are discussed in detail.

1. Chang TY, Bridges TJ (1970) Laser action at 452, 496, and 541 μm in optically pumped CH_3F. *Opt Commun* 1:423–426.
2. Hodges DT, Tucker JR, Hartwick TS (1976) Basic physical mechanisms determining performance of the CH_3F laser. *Infrared Phys* 16:175–182.
3. Henningsen J, Jensen H (1975) The optically pumped far-infrared laser: Rate equations and diagnostic experiments. *IEEE J Quantum Electron* 11:248–252.
4. Dangoisse D, Glorieux P, Wascat J (1981) Diffusion and vibrational bottleneck in optically pumped submillimetre lasers. *Int J Infrared Millimeter Waves* 2:215–229.
5. Matteson W, De Lucia F (1983) Millimeter wave spectroscopic studies of collision-induced energy transfer processes in the $^{13}CH_3F$ laser. *IEEE J Quantum Electron* 19:1284–1293.
6. Tobin MS (1985) A review of optically pumped NMMW lasers. *Proc IEEE* 73:61–85.
7. Everitt HO, Skatrud DD, De Lucia FC (1986) Dynamics and tunability of a small optically pumped cw far-infrared laser. *Appl Phys Lett* 49:995–997.
8. McCormick RI, De Lucia FC, Skatrud DD (1987) A time-resolved study of rotational and vibrational excitation and relaxation in the $^{13}CH_3F$ optically pumped far-infrared laser. *IEEE J Quantum Electron* 23:2060–2068.
9. McCormick RI, Everitt HO, De Lucia FC, Skatrud DD (1987) Collisional energy transfer in optically pumped far-infrared lasers. *IEEE J Quantum Electron* 23:2069–2077.
10. Everitt HO, De Lucia FC (1989) A time-resolved study of rotational energy transfer into A and E symmetry species of $^{13}CH_3F$. *J Chem Phys* 90:3520–3527.
11. Douglas NG (1989) *Millimetre and Submillimetre Wavelength Lasers: A Handbook of CW Measurements* (Springer Berlin), Vol 61.
12. Everitt HO, De Lucia FC (1990) Rotational energy transfer in CH_3F: The $\triangle J = n$, $\triangle K = 0$ processes. *J Chem Phys* 92:6480–6491.
13. Chua SL, et al. (2011) Spatio-temporal theory of lasing action in optically-pumped rotationally excited molecular gases. *Opt Express* 19:7513–7529.
14. Tonouchi M (2007) Cutting-edge terahertz technology. *Nat Photon* 1:97–105.
15. Ferguson B, Zhang XC (2002) Materials for terahertz science and technology. *Nat Mater* 1:26–33.
16. Siegel PH (2002) Terahertz technology. *IEEE Trans Microwave Theory Tech* 50:910–928.
17. Button KJ (2013) *Reviews of Infrared and Millimeter Waves: Optically Pumped Far-Infrared Lasers* (Springer Science & Business Media, New York), Vol 2.
18. Johnson A, Auston D (1975) Microwave switching by picosecond photoconductivity. *IEEE J Quantum Electron* 11:283–287.
19. Van Exter M, Grischkowsky D (1990) Optical and electronic properties of doped silicon from 0.1 to 2 THz. *Appl Phys Lett* 56:1694–1696.
20. Andronov AA, et al. (1978) The gyrotron: High-power source of millimetre and submillimetre waves. *Infrared Phys* 18:385–393.
21. Faist J, et al. (1994) Quantum cascade laser. *Science* 264:553–555.
22. Williams BS (2007) Terahertz quantum-cascade lasers. *Nat Photon* 1:517–525.
23. Saleh BEA, Teich MC (1991) *Fundamentals of Photonics* (Wiley, New York), Vol 22.
24. Everitt HO, De Lucia FC (1995) Rotational energy transfer in small polyatomic molecules. *Adv At Mol Opt Phys* 35:331–400.
25. Everitt HO, III (1990) Collisional energy transfer in methyl halides. PhD thesis (Duke University, Durham, NC).
26. Panock R, Temkin R (1977) Interaction of two laser fields with a three-level molecular system. *IEEE J Quantum Electron* 13:425–434.
27. Bansal R (2006) *Fundamentals of Engineering Electromagnetics* (CRC Press, Boca Raton, FL).

Supplementary Information for

A high-efficiency regime for gas-phase terahertz lasers

Wang et al.

Fan Wang, Steven G. Johnson, Henry O. Everitt, John D. Joannopoulos.
E-mail: wangfan@mit.edu, stevenj@math.mit.edu, everitt@phy.duke.edu, joannop@mit.edu.

This PDF file includes:

> Supplementary text
> Figs. S1 to S7
> References for SI reference citations

Supporting Information Text

1. Experimental Measurements and Theoretical Modeling

In this section, details of experimental measurements and theoretical modeling are provided.

Experimental measurements. The pump beam from a grating-tuned Apollo CO_2 laser (Model 570), producing as much as 15W on the 9P(32) line at 9.657 μm, was focused through a 1mm diameter pinhole in a gold-coated copper plate by a 10cm focal length ZnSe lens into the 0.5cm diameter, 14.3cm long OPFIR laser cavity with a base pressure of $< 10^{-4}$ Torr and a transmitted laser power 2/3 of the incident power (e.g. 10W input pump power at maximum output). The cavity was composed of copper tubing with a gold-coated cylindrical copper plunger inserted into the rear of the cavity to adjust the cavity length while using a bellows to maintain a vacuum seal. In each measurement for a given pressure and pump power, the plunger was adjusted to tune the cavity resonance either to the direct or refilling transition, then the detuning of the CO_2 laser was adjusted with a piezoelectric transducer mounted on a pump cavity mirror to maximize the OPFIR laser output intensity. The 1.2mm wavelength laser radiation strongly diffracted from the 1mm diameter pinhole, so only a fraction was captured for detection through a series of copper pipes, copper mirrors, and Teflon lenses. Attenuators with unknown absorbance were used to limit the power reaching the detector to ensure it remained in the linear-response regime. A Virginia Diodes heterodyne receiver operating in the 220–330GHz band was used to measure the frequency and strength of the OPFIR laser emission. The width of the measured emission lines was less than 3MHz, determined not by the laser but by the detection bandwidth of the spectrum analyzer used to display the intermediate frequency.

Theoretical model. The infrared pump creates non-thermal rotational populations N_ℓ^r and non-equilibrium populations of vibrational thermal pools N_p^v, and the theoretical goal is to predict these differences N from the equilibrium (unpumped) populations and their consequences for THz gain. Our semiclassical theoretical model consists of a set of rate equations giving $\dot{N} = \partial N/\partial t$ for both N_ℓ^r and N_p^v. Below, we begin by describing these rate equations (which include various transitions, coupling to the pump, and an effective-temperature model for unknown vibrational levels), then explain how the $\dot{N} = 0$ steady state is found, and finally how the output power is extracted self-consistently from the populations. Additional technical details are presented in Section 2.

The **rotational-level rate equations** for the symmetry type A being pumped are given by:

$$
\begin{aligned}
\dot{N}_\ell^r(v, \mathbf{r}, t) = \sum_{\ell'} &-\gamma_{\ell\ell'} N_\ell^r(v, \mathbf{r}, t) + \gamma_{\ell'\ell} N_{\ell'}^r(v, \mathbf{r}, t) \\
&- \left(\gamma_{\ell p}^{\mathrm{SPT}} + \gamma_{\ell p}^{\mathrm{VS}} \right) N_\ell^r(v, \mathbf{r}, t) \\
&+ R_{\mathrm{pump}}(v, \mathbf{r}, t) \\
&+ D\nabla^2 N_\ell^r(v, \mathbf{r}, t).
\end{aligned} \tag{1}
$$

Here, population density $N_\ell^r(v, \mathbf{r}, t)$ depends on molecular axial (the direction of the pump beam) velocity v, position $\mathbf{r}$, time t, and energy level ℓ. Because the problem is axisymmetric, we simplify $\mathbf{r}$ to only the radial position, eliminating the axial dependence by an averaging procedure described in Section 2. The first two terms in equation (1) describe dipole–dipole collisions, with $\gamma_{\ell\ell'}$ denoting the transition rate from $\ell \to \ell'$, obtained from $\gamma_{\ell\ell'} = \gamma_{\mathrm{DD}}\rho_{ll'}$. Here, $\gamma_{\mathrm{DD}} = n_{\mathrm{tot}}\langle v_{\mathrm{rel}}\rangle \sigma_{\mathrm{DD}}$, where n_{tot} is the total population density, $\langle v_{\mathrm{rel}}\rangle$ is the thermally averaged relative velocity between molecules, and σ_{DD} is the dipole–dipole collision cross section measured to be 320Å^2 between adjacent rotational levels (1). $\rho_{ll'}$ is the appropriate branching ratio with Boltzmann term. In our case, $\rho_{J \to J+1} = \frac{(J+1)^2 - K^2}{(J+1)(2J+1)}e^{-\frac{\Delta E}{k_B T}}$, and $\rho_{J \to J-1} = \frac{J^2 - K^2}{J(2J+1)}$, in which J and K are rotational quantum numbers, and ΔE is the energy difference between the two rotational levels (4).

The second line in equation (1) describes both a symmetry-preserving thermalization (SPT) process that moves non-thermal population in rotational level ℓ to its associated vibrational thermal pool p with the same A or E symmetry type (2), and a slower "V-swap" (VS) process that moves non-thermal rotational population to both A and E thermal pools with an equal probability (2). Their cross sections are (2, 3) $\sigma^{\mathrm{SPT}} = 137$Å^2 and $\sigma^{\mathrm{VS}} = 21$Å^2 at room temperature.

The $R_{\mathrm{pump}}(v, \mathbf{r}, t)$ term involves only levels L and U as the L→U transition rate induced by absorption of the pump laser (4):

$$
R_{\mathrm{pump}}(v, \mathbf{r}, t) = \left[N_{\mathrm{L}}^{\mathrm{tot}}(v, \mathbf{r}, t) - \frac{g_{\mathrm{L}}}{g_{\mathrm{U}}} N_{\mathrm{U}}^{\mathrm{tot}}(v, \mathbf{r}, t) \right] p_{\mathrm{L} \to \mathrm{U}} \cdot (\delta_{l,\mathrm{U}} - \delta_{l,\mathrm{L}}), \tag{2}
$$

in which $N_{\mathrm{L}}^{\mathrm{tot}}(v, \mathbf{r}, t)$ and $N_{\mathrm{U}}^{\mathrm{tot}}(v, \mathbf{r}, t)$ are the sum of non-thermal and thermal population for levels L and U, g_{L} and g_{U} are the degeneracy of the two levels, and the transition probability is given by

$$
p_{\mathrm{L} \to \mathrm{U}} = \frac{8\pi^3}{3h^2c} \frac{|\langle J', K, V+1|\mu|J, K, V\rangle|^2}{\pi R^2} \left[P_{\mathrm{pump}}^{\mathrm{forw}} f_b^{\mathrm{forw}}(\nu, \nu_p) + P_{\mathrm{pump}}^{\mathrm{back}} f_b^{\mathrm{back}}(\nu, \nu_p) \right]. \tag{3}
$$

Here, h is the Planck constant, c is the speed of light, R is the cell radius, $|\langle J', K, V+1|\mu|J, K, V\rangle|^2$ is the measured (4) dipole matrix element 0.027 Debye^2 for the pump transition, P_{pump} is the effective z-averaged pump power, and $f_b(\nu, \nu_p)$ is the area-normalized lineshape function including pressure (5) and AC-Stark (6) broadening. Both forward (incident direction of

pump beam, or $+z$) and backward ($-z$) directions are included due to the reflection of the back mirror. The formulae for P_{pump} and $f_b(\nu, \nu_p)$ are further discussed in Section 2.

The final term in equation (1) describes the spatial diffusion with a diffusion coefficient $D = \frac{1}{3}\langle v_{\text{abs}}\rangle \ell_{\text{mf}}$ where $\langle v_{\text{abs}}\rangle$ is the averaged absolute velocity and ℓ_{mf} is the mean free path (7). We discretized the diffusion equation with a second-order finite-difference approximation in cylindrical coordinates and with a spatial resolution $10\mu m$ divided by pressure/Torr (since higher pressures have smaller ℓ_{mf} that requires finer resolution), with boundary conditions described below. As mentioned above, we approximate the populations as uniform in z with an averaged pump power, which is accurate in the optimal regime where the pump intensity mostly "fills" the cavity, and allows us to solve only a 1d (radial) diffusion equation.

The **rate equations for the vibrational thermal pools** are dominated by collisions with the cell walls (which introduces a radial dependence) and inter-molecular collisions. For a symmetry type S ($=$ A or E), they are:

$$
\begin{aligned}
\dot{N}^{\text{v}}_{p,S}(\mathbf{r}, t) = \sum_{p'} & -\gamma_{pp'} N^{\text{v}}_{p,S}(\mathbf{r}, t) + \gamma_{p'p} N^{\text{v}}_{p',S}(\mathbf{r}, t) \\
& + \dot{N}^{\text{VS}}_{p,S}(\mathbf{r}, t) \\
& + \sum_{\ell} \left[\delta_{S,\text{A}} \gamma^{\text{SPT}}_{\ell p} + \frac{\gamma^{\text{VS}}_{\ell p}}{2} \right] \int dv N^{\text{r}}_{\ell}(v, \mathbf{r}, t) \\
& + D\nabla^2 N^{\text{v}}_{p,S}(\mathbf{r}, t).
\end{aligned}
\tag{4}
$$

(Unlike the rotational populations, we do not distinguish the vibrational levels $N^{\text{v}}_{p,S}$ by axial velocity v since they do not directly absorb the pump.) The first two terms describe the intermolecular collision between vibrational level $p \to p'$ and vice versa, for instance between V_3 and V_6 with a cross section $\sigma_{V_6 \to V_3} = 3.21\text{Å}^2$ (2). V-swap transitions also occur among vibrational states, described by the second line in equation (4). We consider the most common form of this collision between a V_3A and a V_0E molecule: $V_3\text{A} + V_0\text{E} \leftrightarrow V_0\text{A} + V_3\text{E}$ (2). The third line in equation (4) describes the SPT and VS processes between non-thermal rotational level ℓ and the vibrational thermal pool p, as described in equation (1). The final term describes the diffusion process similar to above.

Although we use a standard Neumann boundary condition ($\partial N/\partial r = 0$) for rotational levels to represent impermeable walls, we define a different vibrational-level boundary condition that expresses relaxation via molecule–wall collisions. Similar to previous work (7), we assume that wall collisions "thermalize" the vibrational levels and redistribute molecules into all possible vibrational levels of the same symmetry S according to a Boltzmann distribution characterized by T_{wall}. Similar to "surface-reaction" boundary conditions used in chemistry (8), we use a Robin boundary condition:

$$
-D\frac{\partial N_p}{\partial r} = \bar{v}(1 - q_p)N_p/2 - \bar{v}q_p \sum_{p' \neq p} N_{p'}/2, \quad \text{at} \quad r = R
\tag{5}
$$

in which q_p is the population fraction of vibrational level p for a Boltzmann distribution at the wall temperature ($T_{\text{wall}} = 300\text{K}$) and $\bar{v}$ is the average velocity of the population flux perpendicular to the wall. A detailed derivation in Section 2 shows $\bar{v} = \langle v_{\text{abs}}\rangle/2$. There is an extra factor of $1/2$ in equation (5) because only half of the population is moving towards the wall. (Note that the diffusion term $D\nabla^2 N$ already captures motion of molecules to/from the wall, so the purely local boundary condition here is more correct than the nonlocal collision rate used in past work (7).)

Effective vibrational temperature (EVT) model. As mentioned in the main text, more higher-lying vibrational levels must be included in the high-pressure regime. Although the energies of these vibrational levels are known (4), the millions of relaxation processes among them are infeasible to measure. To solve this problem, we propose to model all accessible vibrational levels with one expandable thermal pool V_Σ which contains all 120 vibrational levels higher than V_3 up to 6959 cm^{-1} ($\sim 35k_B T_{\text{wall}}$), taking into account the specific energies and degeneracies of each. We argued in the main text that due to fast relaxation processes, all vibrational levels satisfy a Boltzmann distribution with a spatially varying temperature T_v that is determined self-consistently by the population density of V_0 and V_3 for both A and E symmetries: $T^S_v = -\frac{\Delta E}{k_B} \frac{1}{\log\left(N^{\text{tot}}_{3,S}/N^{\text{tot}}_{0,S}\right)}$ where $\Delta E = E_3 - E_0$ is the energy difference between V_3 and V_0. In order to maintain the Boltzmann distribution for V_Σ, we introduce transition rates between V_3 and V_Σ that satisfy $\frac{\gamma_{3\to\Sigma}}{\gamma_{\Sigma\to3}} = \exp\left(\frac{E_3 - \sum_{k \in V_\Sigma} g_k E_k}{k_B T^S_v}\right)$, and, by taking the limit $\gamma_{3\to\Sigma}, \gamma_{\Sigma\to3} \to \infty$, we obtain $N_{\Sigma,S}(r) = \exp\left(\frac{E_3 - \sum_{k \in V_\Sigma} g_k E_k}{k_B T^S_v}\right) N_{3,S}(r)$ for the steady state.

Numerical Solver. The nonlinear rate equations are solved directly by setting $\dot{N}_\ell = 0$ and $\dot{N}_p = 0$ in Eqs. (1, 4). The nonlinearity of the rate equations arises from the pump term, V-swap collision between vibrational levels, and the EVT model. Our nonlinear solver is based on fixed-point iteration with Anderson acceleration (9), which is convenient because it does not require us to compute an explicit Jacobian matrix and makes it easy to add new physics and modify the $\dot{N}$ equations. Typically, we have $\approx 5 \times 10^5$ degrees of freedom (20 energy levels $\times$ 50 radial points $\times$ 500 velocity subclasses). The solution typically converges within 20 Anderson iterations.

Output power. The lasing output power can be obtained by matching terahertz absorption α_{THz} with the gain:

$$\alpha_{\text{THz}} = \frac{\int_V \gamma(\nu, r)|\mathbf{E}(r)|^2 d\mathbf{r}}{\int_V |\mathbf{E}(r)|^2 d\mathbf{r}}, \qquad [6]$$

where α_{THz} is the cavity loss, including ohmic loss and leakage through the front window. Ohmic loss can be computed analytically for the modes of a hollow metal waveguide (10), and the lowest-loss mode is TE_{01}, but which mode lases will depend on the degree of radial and frequency overlap between the gain and mode profiles. As discussed in the main text, the lasing mode pattern could not be observed directly in the experiment, and we used the α_{THz} from TE_{01} for all curves except for refilling lasing with input pump power 6.6W. The 6.6W experimental refilling curve exhibited a jump in amplitude compared to adjacent powers, and we believe that this is due to a different mode being excited by a mistuned cavity; using α_{THz} and the mode profile from TE_{22} best fit the data, indicating that the model could enable us to determine which mode is lasing without directly measuring the mode profile! Since the gain is a small perturbation ($< 0.01\%$) to the permittivity, the electric field $\mathbf{E}(r)$ is accurately approximated by the passive waveguide mode. For convenience, we normalize the mode so that $\int_V |\mathbf{E}(r)|^2 d\mathbf{r} = \int_V d\mathbf{r} = V$. The gain coefficient $\gamma(\nu, r)$ at lasing frequency ν and radial position r is then expressed as (5)

$$\gamma(\nu, r) = \int dv \frac{\Delta N(v, r)\sigma(\nu)}{1 + \Phi|\mathbf{E}(r)|^2/\Phi_s} \qquad [7]$$

which includes contributions from all velocity subclasses. $\Delta N(v, r)$ is the population inversion obtained by solving the rate equations, and $\sigma(\nu)$ is the transition cross section: $\sigma(\nu) = \lambda^2 g(\nu)/8\pi t_{\text{sp}}$, where λ is the lasing wavelength, the spontaneous emission lifetime t_{sp} is taken to be 10sec (7), much longer than all other transition lifetimes in the considered system (see Section 2 for a detailed discussion: t_{sp} has little effect on the peak efficiency), and $g(\nu) = \frac{1}{\pi}\frac{\Delta\nu_P}{(\nu - \nu_v)^2 + \Delta\nu_P^2}$ is the pressure-broadening lineshape function (ν_v is the center frequency for molecules with velocity v). Φ_s is the saturated photon flux density: $\Phi_s = 1/\tau_s\sigma(\nu)$, where τ_s is the characteristic time for the lasing transition. Unlike a three- or four-level system in which τ_s can be analytically derived (5), our system requires τ_s to be obtained numerically from the model. A stimulated emission rate w_{st} is introduced between the two lasing levels, and τ_s is obtained by fitting the population inversion as a function of w_{st}: $\Delta N(w_{\text{st}}) = \Delta N(w_{\text{st}} = 0)/(1 + \tau_s w_{\text{st}})$. Once all ΔN, σ, Φ_s and cavity mode $\mathbf{E}(r)$ are known, we numerically solve equation (6) for the intensity of photon flux density Φ by a Newton method. Finally, the THz output power is obtained from $I_o = h\nu AT\Phi/2$, where A is the cross section of the cavity and T is the transmission coefficient, computed by integrating the waveguide mode's Poynting flux over the output pinhole (since the pinhole is comparable to the wavelength; see Section 2). The formula is divided by 2 to count only photons flowing in the outward direction (5).

2. More Technical Details

In this section, more technical details of the theoretical model are provided.

Broadening linewidth

As explained above, $f_b(\nu, \nu_p)$ is the area-normalized lineshape function (including pressure (5) and AC-Stark (6) broadening), ν_p is the pump frequency, and ν is the transition frequency of molecules with axial velocity v. By the Doppler effect, $\nu^{\pm} = (1 \pm v/c)\nu_0$ for the forward (+) and backward (−) directions, where $\nu_0 = 31.04\text{THz}$ is the intrinsic transition frequency between L and U for $^{13}\text{CH}_3\text{F}$. The lineshape function $f_b^{\pm}(\nu^{\pm}, \nu_p)$ is a convolution of pressure and AC-Stark broadening effects:

$$f_b^{\pm}(\nu^{\pm}, \nu_p) = f_p(\nu^{\pm}, \nu_p) * f_S^{\pm}(\nu^{\pm}, \nu_p)$$

where

$$f_p(\nu^{\pm}, \nu_p) = \frac{1}{\pi}\frac{\Delta\nu_P}{(\nu^{\pm} - \nu_p)^2 + \Delta\nu_P^2}$$

is the pressure broadening (with linewidth $\Delta\nu_P = \frac{1}{2\pi\Delta\tau} \approx 15\text{MHz/Torr}$ with $\Delta\tau$ being the mean collision time (4)), and the AC-Stark broadening $f_S^{\pm}(\nu^{\pm}, \nu_p)$ is also approximately Lorentzian with linewidth (6)

$$\Delta\nu_S^{\pm} = \frac{|\langle J', K, V+1|\mu|J, K, V\rangle|}{2\pi\hbar}\sqrt{\frac{2P_{\text{pump}}^{\pm}}{\pi\epsilon_0 cR}} = 0.38\frac{\sqrt{P_{\text{pump}}^{\pm}/\text{Watt}}}{R/\text{cm}}.$$

(Note that the average pump power $P_{\text{pump}}^{\pm}$ is different for the $+z$ direction and the reflected power in the $-z$ direction, as described below.) The convolution of two Lorentzians is also a Lorentzian with the sum of the linewidths, so we obtain

$$f_b^{\pm}(\nu^{\pm}, \nu_p) = \frac{1}{\pi}\frac{\Delta\nu_b}{(\nu^{\pm} - \nu_p)^2 + (\Delta\nu^{\pm})^2}$$

with

$$\Delta\nu^{\pm} = \Delta\nu_p + \Delta\nu_S^{\pm}.$$

Pump absorption coefficient α and the average pump power

The pump absorption coefficient as a function of radial position r is (4)

$$\alpha^\pm(r) = \frac{8\pi^3 \nu_p}{3hc} \left| \langle J', K, V+1 | \mu | J, K, V \rangle \right|^2 \int g^\pm(v) \left[N_L^{\text{tot}}(v, r) - \frac{g_L}{g_U} N_U^{\text{tot}}(v, r) \right] dv$$

in which h is the Planck constant, c is the speed of light, R is the cavity radius, ν_p is the pump frequency, and $\left| \langle J', K, V+1 | \mu | J, K, V \rangle \right|^2$ is the measured (4) dipole matrix element 0.027 Debye^2 for the pump transition. In the integral over velocity, $g^\pm(v) = f_b^\pm(\nu^\pm(v), \nu_p)$ denotes the pump absorption spectrum for molecules with axial speed v, so that $g^\pm(v)$ is larger if the pump frequency is closer to the Doppler-shifted L→U transition frequency at that v. Note that $\alpha^\pm(r)$ is different in forward (+) and backward (−) directions since they have different Doppler shifts and powers. The spatially averaged pump absorption coefficient is obtained by:

$$\alpha^\pm = \frac{\int_0^R \alpha^\pm(r) r \, dr}{\int_0^R r \, dr}.$$

Note that α_p in the main text for the definition of optimal cavity length ($L_o = 1/2\alpha_p$) is the same with α^+. Figure S1 shows IR absorption spectrum α^+ in the forward direction at 100 mTorr and 400 mTorr with various input pump powers. $\nu_0 = 31.0427$ THz is the frequency of the L–U transition, while the CO$_2$ pump laser is incident at a frequency 25 MHz $> \nu_0$. The figure shows a dip at the pump frequency with nonzero pump power because of reduced population in the L state. The width of the dip increases with pressure and pump power, as described in the previous section, becoming so broad at 400 mTorr that its effect is hard to see. There is an extra dip at -25MHz due to the Doppler-shifted pump reflection at the back mirror of the cavity.

Since the pump photon can travel back and forth inside the cavity, reflecting off of the front and back gold-coated copper mirrors, we sum all the trips to obtain an effective z-averaged pump power in each direction. The loss for one round trip is $\beta = e^{-\alpha^+ L - \alpha^- L} R_1 R_2$, where $R_2 = 0.95$ is the reflection on the back mirror at IR frequency 31.04THz incident on a gold-coated copper plate, $R_1 = 0.96 \times 0.95$ is the reflection of the front mirror considering an extra 4% leakage from the pinhole. Then the average pump power is computed by a z-averaging procedure:

$$P_{\text{pump}}^+ = \frac{P_0}{1-\beta} \frac{\int_0^L \exp\left(-\alpha^+ z\right) dz}{L} = \frac{P_0}{1-\beta} \frac{1 - \exp(-\alpha^+ L)}{\alpha^+ L}$$

$$P_{\text{pump}}^- = \frac{P_0 R_2 \exp(-\alpha^+ L)}{1-\beta} \cdot \frac{1 - \exp(-\alpha^- L)}{\alpha^- L}$$

where P_0 is the input pump power. The average pump power decreases as pressure and IR absorption coefficient increase for a given input pump power.

Unphysical bottlenecking at high pressures

As mentioned in the main text, the reason why previous models produced unphysical bottlenecking at high pressures was conjectured to be their inclusion of only a few vibrational levels. Here, we demonstrate this unphysical bottlenecking phenomena by including all the rotational levels as shown in Fig. 1 of the main text, but only the 6 vibrational levels that are most directly connected to the lasing energy levels. In this 6-level model, we used measured transition rates between the vibrational levels, and all of the collisional and diffusion processes mentioned in the main text were included. The *only* difference is that it has no effective temperature to model the "missing" higher-lying vibrational levels, and the population of all 6 vibrational levels is solved exactly. The output THz powers with different input pump powers (3.3W, 6.6W, and 10W) are shown in Fig. S2. A clear pressure bottlenecking is seen around 700 mTorr, above which no lasing is achieved. This confirms the long-held understanding that including only few vibrational levels in the model induces the unphysical high-pressure quenching of the inversion through vibrational bottlenecking.

Radial distribution of population inversion and effective temperature T_v

The radial distribution of the population inversion ΔN_U for the direct transition at 100 mTorr, 200 mTorr, 400 mTorr, and 1 Torr with 10W input pump power is plotted in Fig. S3. Since the primary pathway for vibrational relaxation is molecule–wall collisions, the population inversion is larger at radial positions closer to the cavity wall, as shown in the figure. This effect is crucial for cavity design.

The effective vibrational temperature T_v provides a deeper understanding of the system dynamics. Figure S4 shows a contour plot of T_v for the A-type vibrational thermal pools as a function of radial position and molecular pressure, for an input pump power of 10W and a cavity length $L = 14.3$cm. The effective vibrational temperature is higher in the cell center, where the pump is more saturated and the gain is smaller. One would normally expect T_v to increase with pressure due to faster intermolecular collisions, but in this figure T_v actually *decreases* above 400 mTorr because the z-averaging of the pump power lowers the pump rate and brings the effective temperature down. If we plot the T_v with optimal cavity length (which decreases with pressure so that the whole cavity remains pumped) as discussed in the main text, the result (shown in Fig. S5) exhibits effective temperatures that increase with pressure as expected.

THz gain spectrum

The small-signal gain spectrum is computed as

$$\gamma_0(\nu) = \int dv \, \langle \Delta N(v) \rangle \, \sigma(\nu)$$

where $\langle \Delta N(v) \rangle$ is the spatially averaged population inversion of velocity subclass v, and $\sigma(\nu)$ is the transition cross section (see Section 1). Typical gain spectra are plotted in Fig. S6 at 100 mTorr and 400 mTorr with the input pump power equal to 3W and 10W. The width of THz gain spectrum is proportional to the gas pressure due to pressure broadening. Such flat gain profiles at high pressures potentially allow the THz lasing frequency to be tuned over a correspondingly broad range ($\sim \pm 10$ MHz at a few hundred mTorr) without sacrificing efficiency.

Spontaneous-emission lifetime

To compute the gain coefficient and the output power, the spontaneous emission lifetime t_{sp} is taken to be 10 seconds in Section 1. In fact, the precise value of t_{sp} has little effect on the peak output power far above threshold. In this section, we first demonstrate the effect of t_{sp} by explicit numerical calculations (re-running our model with different values of t_{sp}, shown in Figure S7), and then we present a simple analytical explanation for the lack of influence of t_{sp}.

Figure S7 shows the numerical output power of both direct (solid lines) and refilling (dashed lines) lasing as a function of pressure with the input pump power equal to 10W, and with three different spontaneous emission lifetimes t_{sp}: 1sec (blue), 10sec (red), and 100sec (green). The output power curves are very close, especially in the high-power regions far above the threshold, for both direct and refilling inversions. The biggest effect of t_{sp} is on the high-pressure cutoff for the direct transition, but in this (uninteresting, low-efficiency) high-pressure regime our model's z-averaging assumption is inaccurate as discussed in the main text.

It is straightforward to show analytically that the effect of t_{sp} approximately cancels in the high-power regime. In that regime, far above threshold, $\Phi \gg \Phi_s$, and Eq. (5) from the main text becomes

$$\alpha_{\mathrm{THz}} \approx \frac{1}{V} \int \int \frac{\Delta N(v) \, \sigma(\nu)}{\Phi \, \tau_s \, \sigma(\nu)} \, dv \, d\mathbf{r} = \frac{\langle \Delta N \rangle}{\Phi \tau_s}$$

where $\langle \Delta N \rangle$ is the spatially averaged population inversion and σ is the transition cross section (which depends on t_{sp}). This equation yields an approximate flux density $\Phi \approx \langle \Delta N \rangle / \tau_s \alpha_{\mathrm{THz}}$, in which σ has cancelled and therefore the dependence on t_{sp} has vanished.

Average velocity of the population flux into the wall

The boundary condition for the vibrational levels, discussed in Section 1, is written in terms of $\bar{v}$, the average molecule speed in the direction perpendicular to the wall (say, $+x$). In this section, we briefly review the computation of $\bar{v}$ by standard methods. In particular, the molecule velocities follow a Maxwell–Boltzmann distribution

$$f_{\mathrm{MB}}(v_x) = \sqrt{\frac{m}{2\pi k_B T}} e^{-\frac{m v_x^2}{2 k_B T}}$$

By averaging the velocities in the $+x$ direction, one obtains

$$\bar{v} = \frac{\int_0^\infty v_x f_{\mathrm{MB}}(v_x) dv_x}{\int_0^\infty f_{\mathrm{MB}}(v_x) dv_x} = 2 \int_0^\infty v_x f_{\mathrm{MB}}(v_x) dv_x$$

$$= \sqrt{\frac{m}{2\pi k_B T}} \int_0^\infty e^{-\frac{m v_x^2}{2 k_B T}} d(v_x^2) = \sqrt{\frac{2 k_B T}{\pi m}}.$$

On the other hand, the average absolute velocity is

$$\langle v_{\mathrm{abs}} \rangle = \left(\frac{m}{2\pi k_B T} \right)^{3/2} \int |\mathbf{v}| \exp\left(-\frac{m v^2}{2 k_B T} \right) d\mathbf{v} = \sqrt{\frac{8 k_B T}{\pi m}}.$$

Therefore $\bar{v} = \langle v_{\mathrm{abs}} \rangle / 2$.

Transmission through the output pinhole

THz radiation transmitted through the output pinhole affects the calculation of total loss, lasing threshold, and the output power. Instead of using the ratio of pinhole area and the cavity cross section (5), which is only correct for a uniform intensity (e.g. a plane wave), the transmission coefficient T is computed by integrating the waveguide mode's Poynting flux over the output pinhole. (This is also an approximation, which is valid because the 1mm diameter pinhole is not small compared to

1.2mm wavelength. The radiation through a very subwavelength hole would require an entirely different approach ([11]).) For a circular waveguide's TE_{nm} mode ([10]),

$$P_{\text{rad}} = \int_S \frac{1}{2} \operatorname{Re} \left(\mathbf{E} \times \mathbf{H}^* \right)_z d\mathbf{r} = \frac{Z_{nm}^{\text{TE}}}{2} \int_S (|H_r|^2 + |H_\phi|^2) d\mathbf{r}$$

in which $Z_{nm}^{\text{TE}} = (k_0/\beta_{nm})Z_0$ is the modal wave impedance. k_0 is the free space wave number, $\beta_{nm} = \sqrt{k_0^2 - (p'_{nm}/R)^2}$ is the propagation constant, and Z_0 is the vacuum impedance. Here we consider the TE_{01} mode in a circular waveguide, since it has the lowest Ohmic loss. It is straightforward to do a similar analysis for other cavity modes.

The radiated power through an area S for the TE_{01} mode is $P_{\text{rad}} = \frac{Z_{01}^{\text{TE}}}{2} \left(\frac{\beta_{01} p'_{01}}{R k_{c,01}^2} \right)^2 \int_S J_1^2 \left(\frac{p'_{01} r}{R} \right) d\mathbf{r}$ where $p'_{01} = 3.83$ is the first zero of the Bessel function derivative $J_0'(x)$ and $k_{c,01} = p'_{01}/R$ is the wavenumber corresponding to the TE_{01} mode. The total radiation over the whole waveguide cross section is $P_{\text{tot}} = \frac{Z_{01}^{\text{TE}}}{2} \left(\frac{\beta_{01}}{k_{c,01}^2} \right)^2 2\pi \int_0^{p'_{01}} J_1^2(x) x dx = \frac{\pi Z_{01}^{\text{TE}} \beta_{01}^2}{2 k_{c,01}^4} p_{01}'^2 J_0^2(p'_{01})$. In the experiment, the pinhole is centered at $r = 0$ with radius equal to $R/5$, so the radiation through the pinhole is $P_{\text{pinhole}} = \frac{\pi Z_{01}^{\text{TE}} \beta_{01}^2}{k_{c,01}^4} \int_0^{p'_{01}/5} J_1^2(x) x dx$. So the effective transmission coefficient is

$$T_{\text{exp}} = \frac{P_{\text{pinhole}}}{P_{\text{tot}}} = \frac{\int_0^{p'_{01}/5} J_1^2(x) x dx}{\int_0^{p'_{01}} J_1^2(x) x dx} \approx 0.016.$$

T_{exp} is smaller than the area ratio 0.04, due to the fact that the Poynting flux of TE_{01} mode is higher around $r = 0.48R$, instead of $r = 0$. This indicates that an off-centered pinhole would give larger transmission, which would increase the lasing efficiency (and the threshold power) by increasing the THz radiation rate compared to the Ohmic loss rate. Here, we compute the optimized transmission coefficient for a pinhole centered at $r = 0.48R$ with the same radius $R/5$:

$$T_{\text{opt}} = \frac{\int_0^{2\pi} \int_0^{R_{\text{pinhole}}} J_1^2 \left(p'_{01} x(r, \theta)/R \right) r dr d\theta}{2\pi \int_0^R J_1^2(p'_{01} r/R) r dr} \approx 0.075,$$

where $x(r, \theta) = \sqrt{r_0^2 + r^2 - 2rr_0 \cos\theta}$ with $r_0 = 0.48R$ is the pinhole center. This enhanced transmission coefficient for an off-center pinhole increases both the output power and the efficiency by decreasing the fraction of power lost to Ohmic absorption.
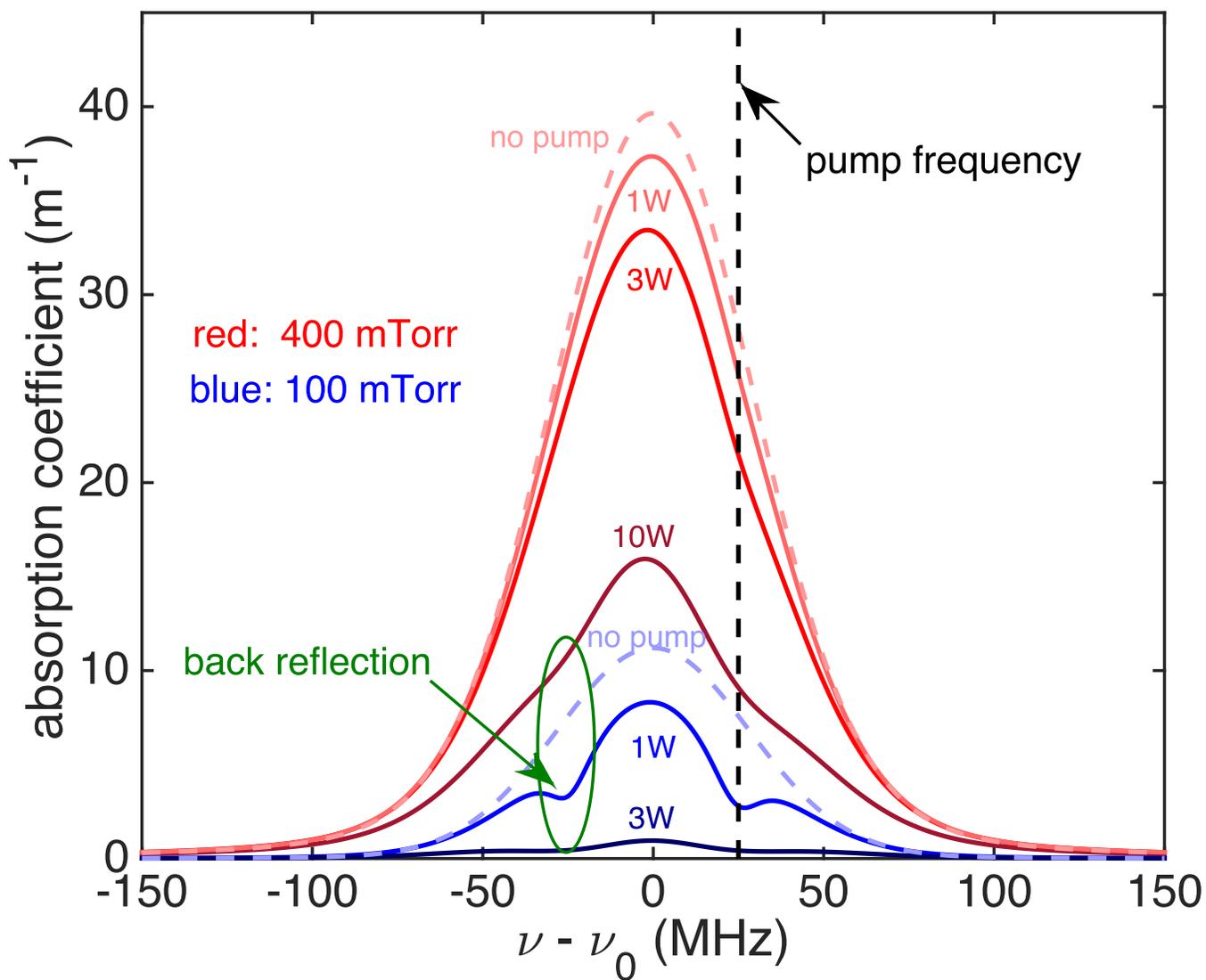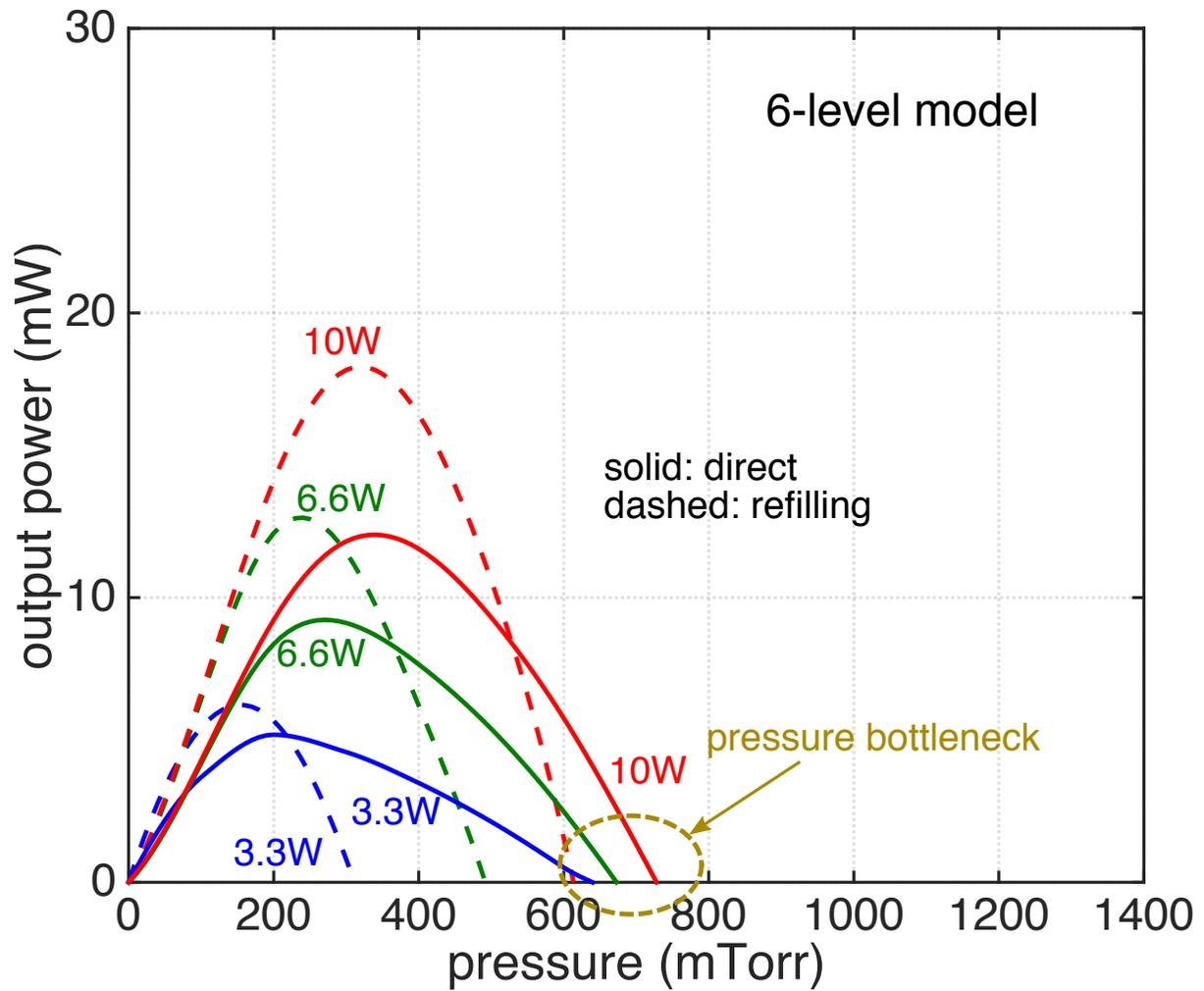
Fig. S1. IR absorption spectrum at 100 mTorr and 400 mTorr with various input pump powers. $\nu_0 = 31.0427$ THz is the frequency of the L–U transition, while the CO_2 pump laser is incident at a frequency $25\,\text{MHz} > \nu_0$.

Fig. S2. THz output power as a function of gas pressure, for various input pump powers (3.3W, 6.6W, and 10W), and for both the direct (solid lines) and refilling (dashed lines) transitions by a 6-level model. It is clearly observed that no gain is obtained above 700 mTorr by the 6-level model, known as high-pressure unphysical bottlenecking.
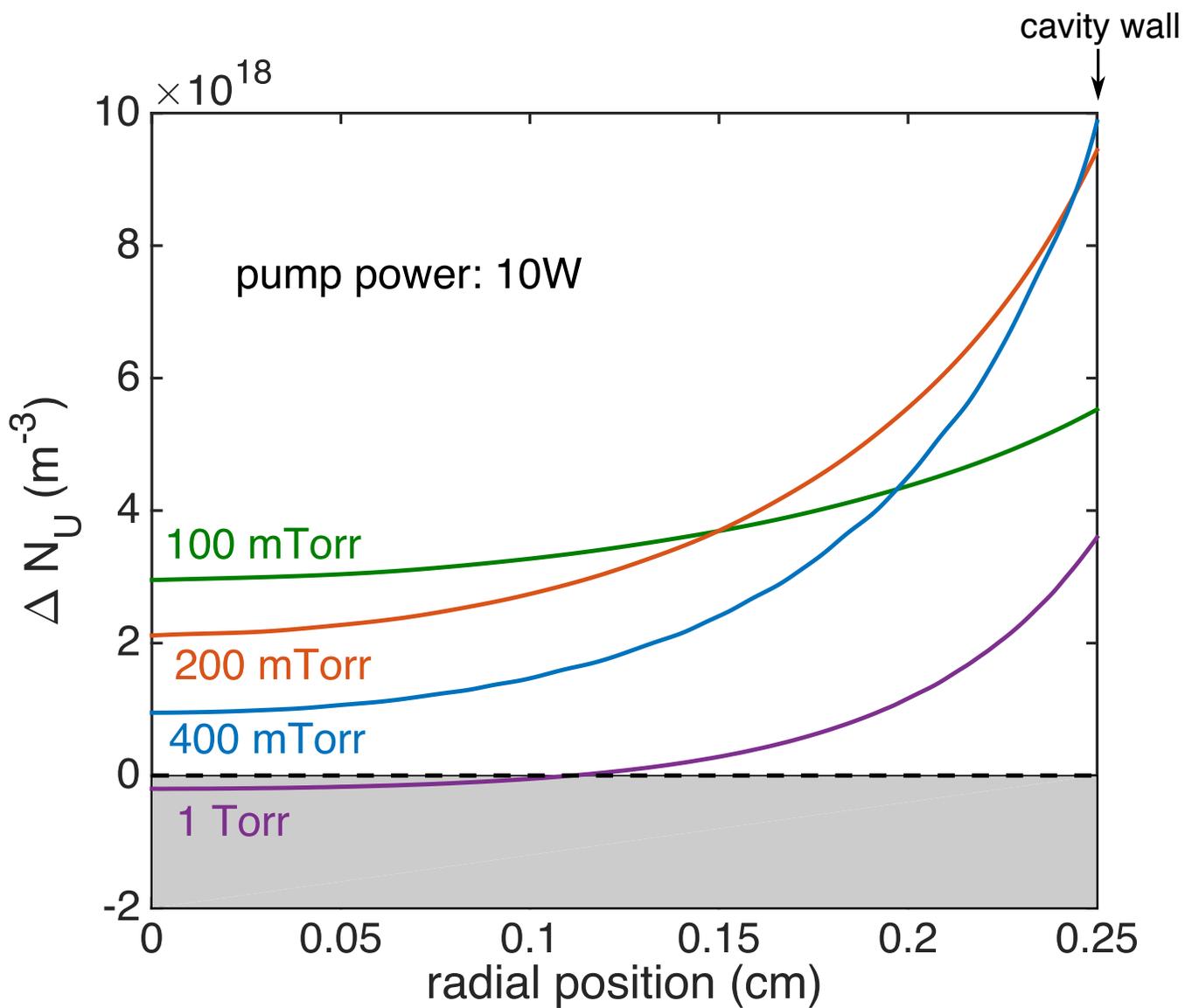
Fig. S3. Radial distribution of population inversion for direct transition at 100 mTorr, 200 mTorr, 400 mTorr, and 1 Torr, with 10W input pump power.
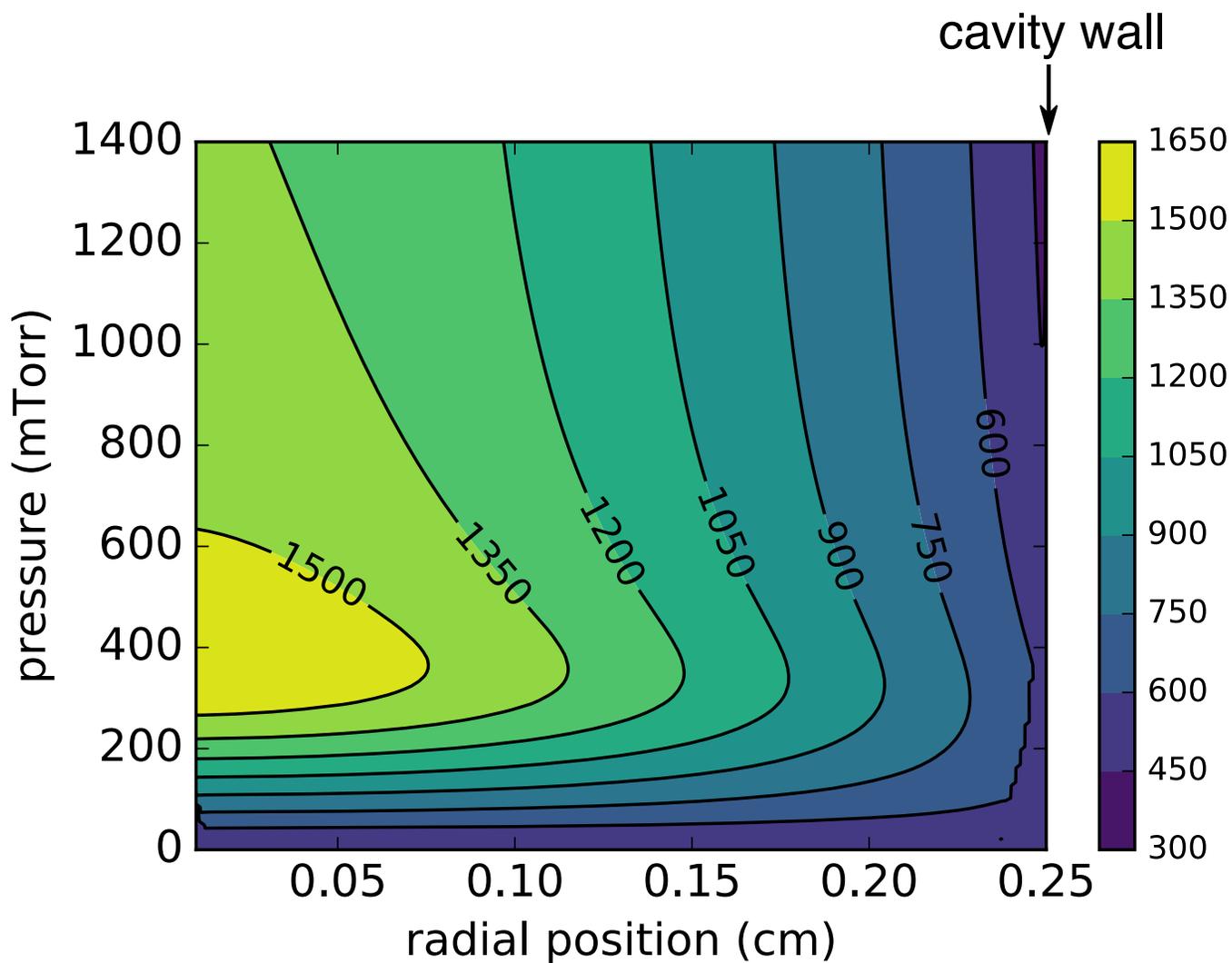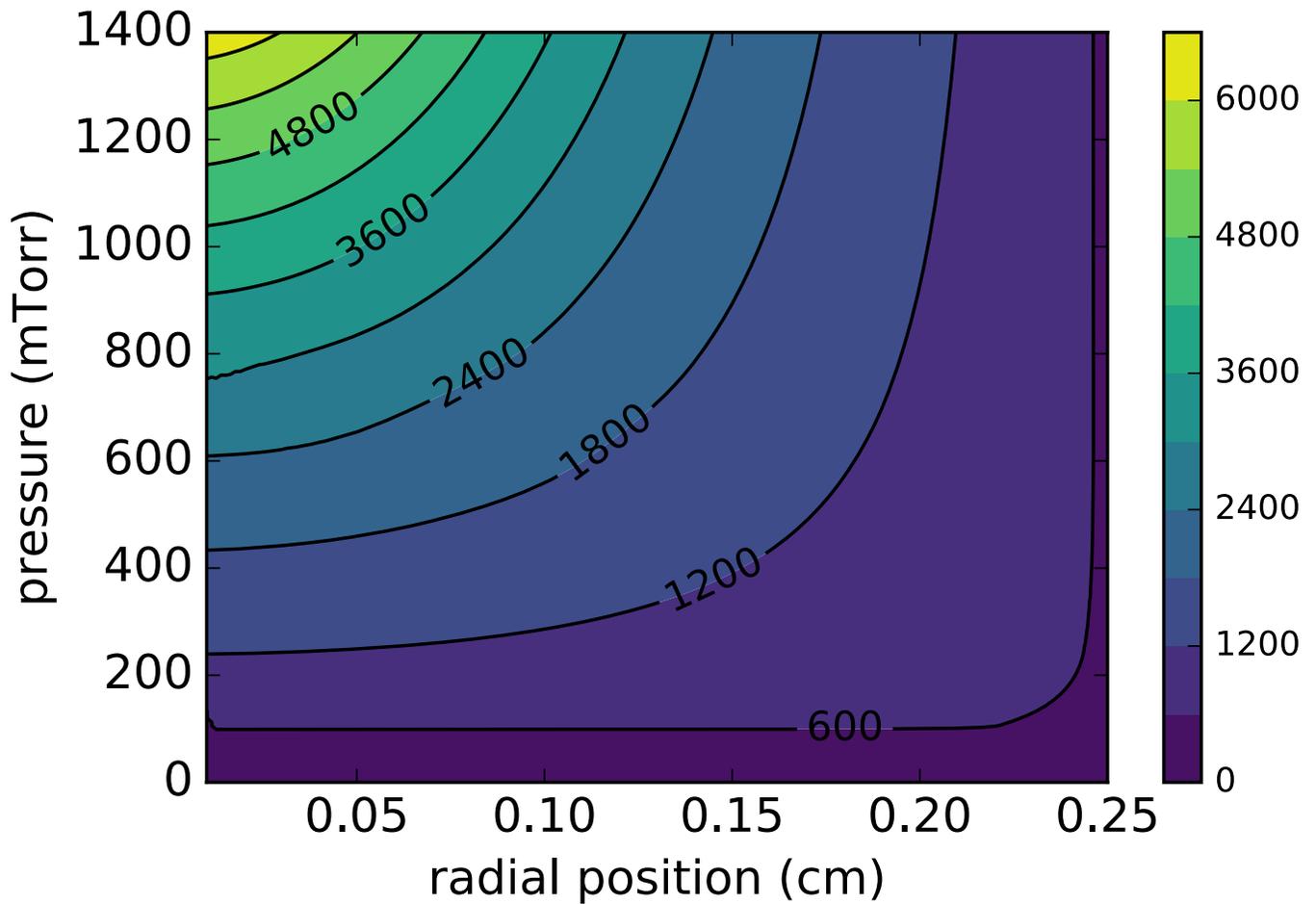
Fig. S4. The effective temperature T_v (in Kelvin) of type-A vibrational thermal pools as a function of radial position and molecular pressure, for an input pump power of 10W. The cavity is 5mm×14.3cm as in experiments.

Fig. S5. The effective temperature T_v (in Kelvin) of type-A vibrational thermal pools as a function of radial position and molecular pressure, for an input pump power of 10W. The cavity length is optimized to match the IR absorption: $L_o = 1/2\alpha_p$, and the cavity diameter is 5mm.
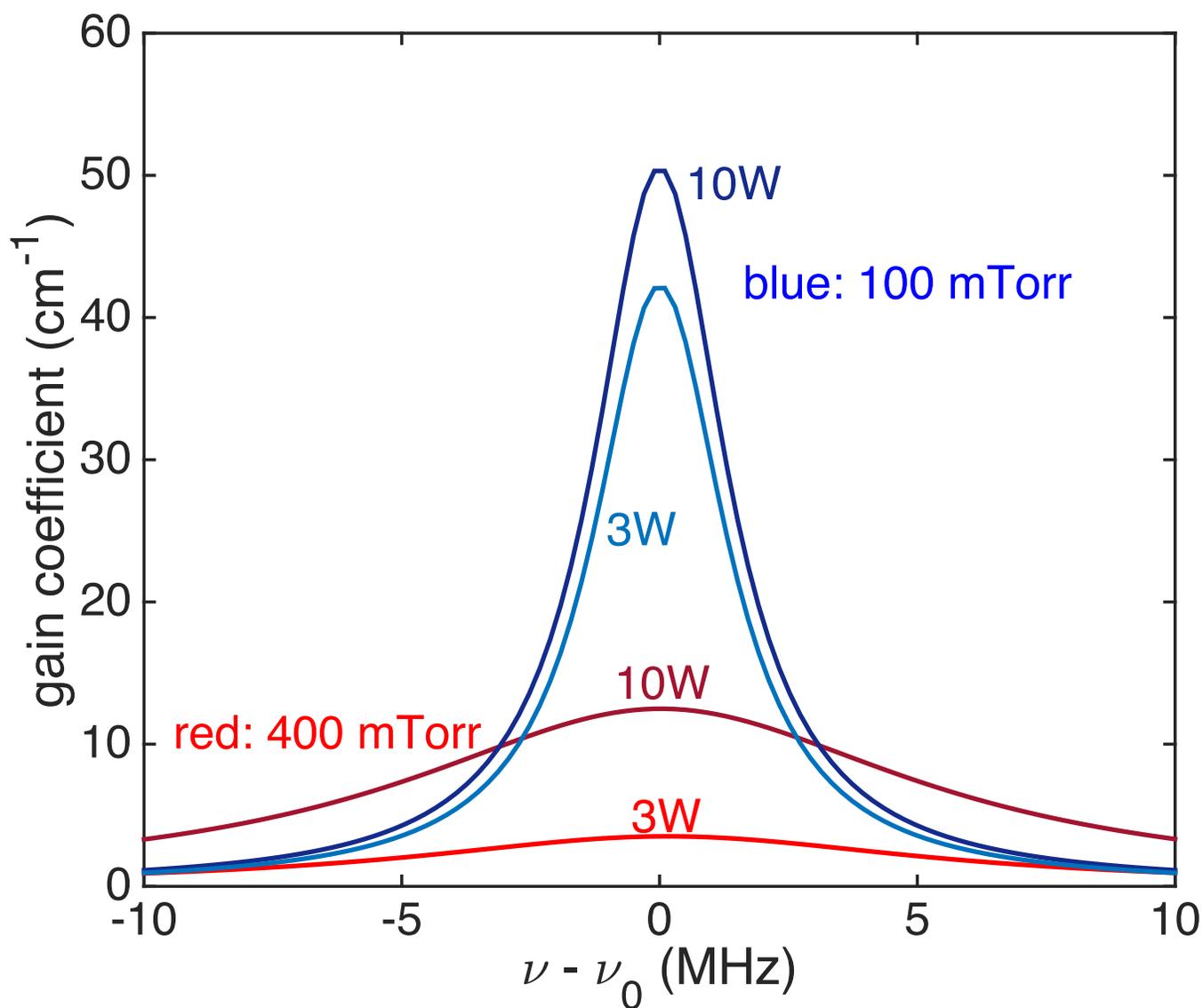
Fig. S6. THz gain spectrum at 100 mTorr and 400 mTorr with the input pump power equal to 3W and 10W. The width of spectrum is proportional to the gas pressure due to pressure broadening.
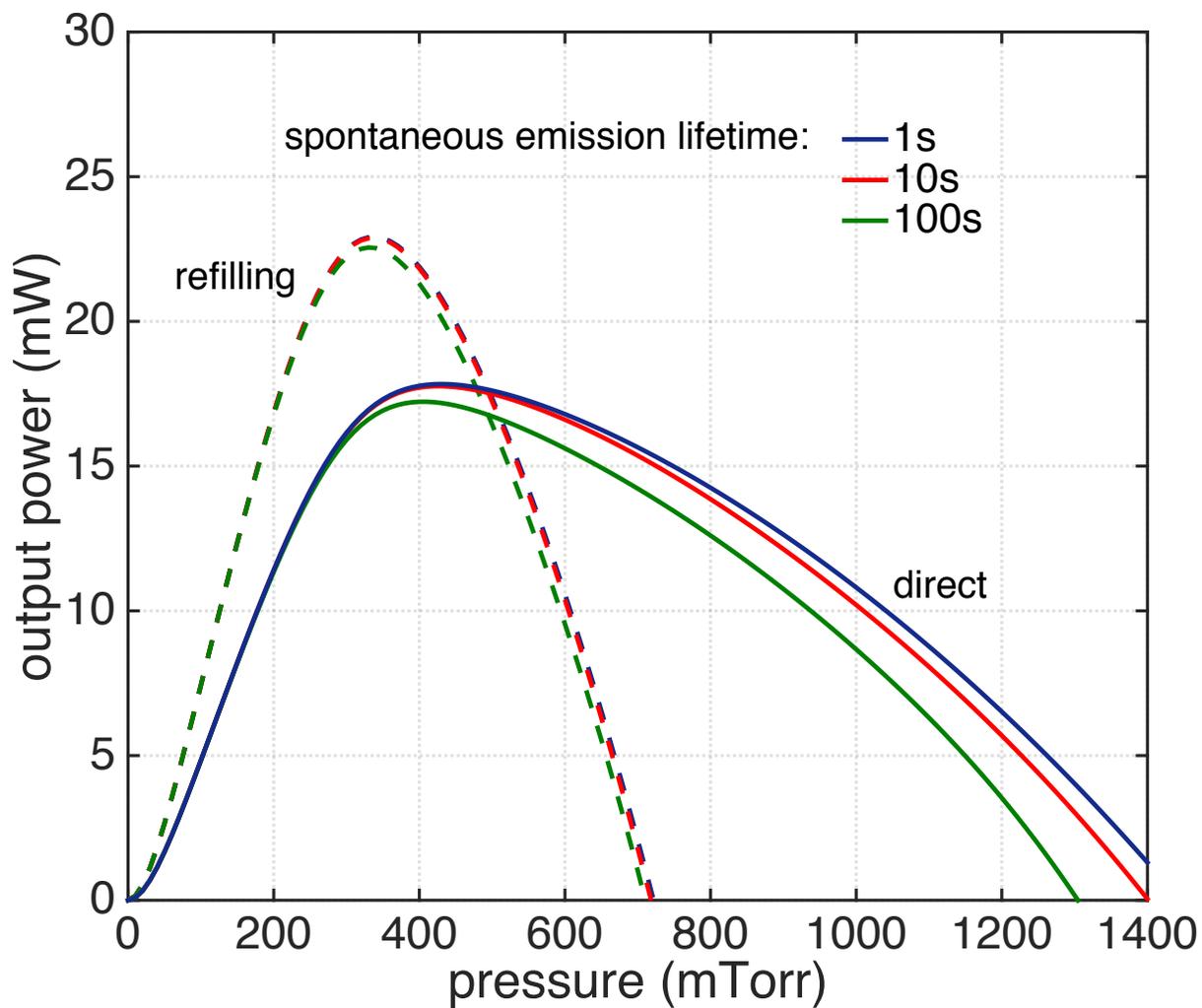
Fig. S7. Numerical output power of both direct (solid lines) and refilling (dashed lines) lasing versus pressure with the input pump power equal to 10W, and with three different spontaneous emission lifetimes $t_{\rm sp}$: 1sec, 10sec, and 100sec. $t_{\rm sp}$ has little effect on the peak output power far above threshold for both lasing transitions.

References

1. Everitt HO, De Lucia FC (1990) Rotational energy transfer in CH$_3$F: The $\Delta J = n$, $\Delta K = 0$ processes. *The Journal of Chemical Physics* 92(11):6480–6491.
2. Everitt HO, De Lucia FC (1989) A time-resolved study of rotational energy transfer into A and E symmetry species of ^{13}CH$_3$F. *Journal of Chemical Physics* 90(7):3520–3527.
3. Everitt HO, De Lucia FC (1995) Rotational energy transfer in small polyatomic molecules. *Advances in Atomic, Molecular, and Optical Physics* 35:331.
4. Everitt III HO (1990) Ph.D. thesis (Duke University).
5. Saleh BEA, Teich MC (1991) *Fundamentals of Photonics*. (Wiley) Vol. 22.
6. Panock R, Temkin R (1977) Interaction of two laser fields with a three-level molecular system. *IEEE Journal of Quantum Electronics* 13(6):425–434.
7. Chua SL, et al. (2011) Spatio-temporal theory of lasing action in optically-pumped rotationally excited molecular gases. *Optics Express* 19(8):7513–7529.
8. Fogler HS (1999) *Elements of Chemical Reaction Engineering*. (Prentice-Hall International London).
9. Walker HF, Ni P (2011) Anderson acceleration for fixed-point iterations. *SIAM Journal on Numerical Analysis* 49:1715–1735.
10. Bansal R (2006) *Fundamentals of Engineering Electromagnetics*. (CRC press).
11. Bethe HA (1944) Theory of diffraction by small holes. *Physical Review* 66(7-8):163.